Speciation of Copper in Spherical Mesoporous Silicates: From the Microscale to Angstrom

7 AUTHORS, INCLUDING:

Leandro Andrini
National University of La Plata. Fac. de Cie...
15 PUBLICATIONS **201** CITATIONS

SEE PROFILE

Mónica Crivello
National University of Technology
27 PUBLICATIONS **442** CITATIONS

SEE PROFILE

Felix Requejo
National University of La Plata
121 PUBLICATIONS **2,371** CITATIONS

SEE PROFILE

Eduardo Herrero
National University of Technology
56 PUBLICATIONS **598** CITATIONS

SEE PROFILE

Speciation of Copper in Spherical Mesoporous Silicates: From the Microscale to Angstrom

Corina M. Chanquía,[†,‡] **Leandro Andrini,**[‡,§] **Julio D. Fernández,**[†] **Mónica E. Crivello,**[†]
Félix G. Requejo,[‡,§] **Eduardo R. Herrero,**[†] **and Griselda A. Eimer**[*,†,‡]

*Centro de Investigación y Tecnología Química (CITeQ), Universidad Tecnológica Nacional, Facultad Regional
Córdoba, Maestro López esq. Cruz Roja Argentina, 5016 Córdoba, Argentina, INIFTA (FCE, UNLP and
CONICET), CC/16 Suc. 4, 1900, La Plata, Argentina, and CONICET, Avenida Rivadavia 1917,
C1033AAJ, Buenos Aires, Argentina*

Received: March 23, 2010; Revised Manuscript Received: June 5, 2010

MCM-41 type mesoporous silicate particles with spherical morphology containing copper nanospecies were synthesized by conventional hydrothermal synthesis. A narrow distribution of silicate particle sizes between 2 and 3 μm and a well-defined mesoporosity were evidenced by electronic microscopy, even for loadings of copper of about 10 wt %. Moreover, CuO nanoparticles $\sim$30 nm in diameter occluded in the amorphous silica, possibly filling some secondary mesoporosity, were also detected. By Fourier transform infrared spectroscopy with pyridine adsorption and UV–vis diffuse reflectance spectroscopy measurements together with reduction experiments under H_2 flow, a detailed study about the relationship between copper loading degree and the acid properties with the local isolated $Cu^{\delta+}$ species surroundings was performed. The incorporation of copper into the silica framework generated surface Lewis acid sites which increase with copper content. The origin of these acid sites could be attributed to the presence of isolated $Cu^{\delta+}$ species possibly coordinated with the framework oxygen atoms. It is noteworthy that Brønsted acid sites were not detected in our materials. By X-ray absorption near edge structure spectroscopy, we determine the coexistence of copper +1 and +2 states. The average coordination numbers calculated from extended X-ray absorption fine structure experiments are consistent with a mixture of nanosized species of copper: CuO nanoparticles, besides isolated $Cu^{\delta+}$ cations located in framework positions with oligonuclear clusters like $[Cu^{\delta+}\cdots O^{\delta-}\cdots Cu^{\delta+}]_n$ in its surroundings, confined within the pores.

Introduction

Significant research on mesoporous silica has occurred since the discovery of M41s type mesoporous materials in 1992.[1,2] In particular, potential applications of the MCM-41 materials—a member of M41s family—require strict control of both the nanoporous structure and their macroscopic morphology. MCM-41 has a hexagonal arrangement of one-dimensional mesopores with diameters of 20–100 Å and is thermally stable at 1100 °C with very high surface areas >900 m²/g. Nowadays, MCM-41 bridges the gap between microporous zeolites and macroporous amorphous silicates in chemical and catalysis applications.[3] Thus, MCM-41 materials have extended the range of catalytic reaction engineering beyond the micropore domain. Therefore, the exploration of new formulations to generate morphologies and controlled particle sizes of these mesoporous silicates is the crucial step to achieve its extensive applications. In 1997, Unger et al.[4] reported the first synthesis of MCM-41 silicate with spherical morphology in the submicrometer size. Later, the same group reported novel pathways controlling the morphology of the product in preparation of MCM-41.[5] They concluded that the addition of alcohol to the reacting mixture led to homogeneous crystallization system favoring the formation of spherical MCM-41 matter. However, the main drawback of these approaches was that the particle size of the obtained products was in submicrometer order and the formation of

mesostructure usually took a long time. Since it is highly desired to apply the MCM-41 type materials to fluidized-bed reactors (FBR) because they can be used to carry out a variety of multiphase catalytic reactions, large-particle mesoporous materials with spherical morphology are demanded.[6]

Reduction of NO_x is of great importance and interest in air pollution control especially in the high-temperature combustion processes. The major NO_x emission sources are fuel combustion in automobile engines and coal-fired power plants. Emissions of nitrous oxide (N_2O) have also received much attention because of its global-warming effects. Generally, NO is much more abundant than other nitrogen oxides in the NO_x pollutants.

On the other hand, CO oxidation is also of prime importance to fundamental studies in catalysis, pollution control, and feed purification for fuel cell applications. To meet increasingly stringent environmental regulations in exhaust emission control, the complete oxidation of carbon monoxide is crucial.[7] CO is also found in ineffective combustion processes.

Catalytic reduction of NO in the presence of CO has been widely studied in the emission control of automobile exhausts.[8–10] Precious metals (Pd, Pt, Rh) have traditionally been used as the most efficient catalysts with high activity and stability for this process. However, owing to the high cost and lack of availability of the precious metals, copper catalysts are of increasing importance in catalytic reduction of NO.[3,11] Copper species introduced onto MCM-41, an inert and well-characterized molecular sieve, should be correlated with their activity in this reaction. In addition, with the ordered framework and relatively large pore diameter of MCM-41, the influence of intraparticle resistance can be neglected when the reaction

12222 *J. Phys. Chem. C, Vol. 114, No. 28, 2010*

Chanquía et al.

kinetics is concerned. However, the metal loading may affect the structure and thus the activity of the resulting catalyst.[3]

Adsorption of weakly interacting small probe molecules in combination with suitable analytical techniques is a widely used procedure to study various properties of catalytic surfaces, among these the acidity−basicity. In such investigations, the observed probe molecules alterations, induced by adsorption, are related to the properties of the exposed sites. When the adsorption of the probe onto the exposed sites is studied from the energetic point of view, the bond strength of the acid−base molecular complex can be determined and it can be related to the strength of the acid site. Vibrational spectroscopy (FT-IR) is the most common technique used, with eminently qualitative nature, in surface acidity studies.[12] In many catalytic reactions, the presence of highly dispersed metal centers, acting as acid Lewis centers, is desired for an enhanced catalytic activity, as in the case of NO_x reactions already studied on these catalysts.[13]

X-ray absorption spectroscopy (XAS) is widely used to study metal-containing porous materials.[14] XAS is an element-specific probe and is especially useful as it targets the element or metal of interest. An XAS spectrum is typically divided into the near edge and edge region called X-ray near-edge spectroscopy (XANES) and the extended X-ray absorption fine structure (EXAFS) extending up to 100 eV above the edge. The XANES region serves as a fingerprint for a qualitative exploration and further analysis allows the determination of averaged coordination and electronic and valence states of absorbing atoms. Careful data manipulation of the EXAFS yields information regarding the atomic sites multiplicity, interatomic distances, thermal disorder (Debye−Waller factor), and in some cases also the type of atom for neighboring shells of the targeted atom. For heterogeneous catalysts, which typically consist of metal-carrier systems or metal incorporated zeotype structures, the amount of metal is not sufficient nor does it show long-range order which allows for conventional characterization by techniques such as X-ray diffraction. However, XAS is particularly useful, as the technique is applicable for crystalline, amorphous and liquid phases.[15] XAS has been extensively used to study local metal environments in a number of zeo-types for their application in NO_x catalytic reduction. Examples include copper-substituted microporous alumino- and silicoaluminophosphates, and the copper-containing zeolite.[3,16−18]

The nature and distribution of copper nanospecies in mesoporous molecular sieves of type MCM-41, as well as their main microstructural and surface characteristics, have been recently presented and discussed by us.[19] The aim of this article is to complete the study of the morphological, structural, and chemical properties of these MCM-41 type mesoporous molecular sieves modified with copper (Cu-MMS). The particle size, morphology, and structural regularity of Cu-MMS have been investigated by electronic microscopy (scanning and transmission). A complete study of absorption of pyridine coupled to FT-IR spectroscopy together with reduction experiments under H_2 flow and DR-UV−vis measures were performed with the purpose of relating the copper loading degree and the acid properties, with the local isolated $Cu^{\delta+}$ species surroundings. XAS measurements were performed in order to extend the study about of the nature of copper species presented in our previous study.

Experimental Section

Catalyst Preparation. The copper-containing mesoporous molecular sieves (Cu-MMS) were prepared by a direct hydrothermal method using cetyltrimethylammonium bromide (CTABr,

Aldrich) as template. Tetraethoxysilane (TEOS, Fluka ≥98%) and copper(II) nitrate ($Cu(NO_3)_2 \cdot 3H_2O$, Anedra) were used as the Si and Cu sources, respectively. The pH of the synthesis was adjusted to 13 by adding tetraethylammonium hydroxide (TEAOH, Sigma-Aldrich), 20 wt % aqueous solution. The catalysts were synthesized from a gel of molar composition: Si/Cu = 20, 60, and 240; TEAOH/Si = 0.3; CTABr/Si = 0.3; H_2O/Si = 60. In a typical synthesis, TEOS and $Cu(NO_3)_2 \cdot 3H_2O$ were vigorously mixed for 30 min. Then a 25 wt % solution of CTABr in ethanol and 70% of the TEAOH were added dropwise; this mixture is continuously stirred for 3 h. Finally, the remaining TEAOH and the water were further added dropwise to the milky solution of light blue color which was then heated at 85 °C for 30 min to remove ethanol used in solution and produced in the hydrolysis of TEOS. This gel was treated hydrothermally into a Teflon-lined stainless-steel autoclave and kept in an oven at 100 °C for 1 day under autogenous pressure. The final solids were filtered, washed with distilled water until pH ∼7, and dried at 60 °C overnight. The color of the as-synthesized samples was light turquoise. The template was evacuated from the samples by heating (2 °C/min) under N_2 flow (45 mL/min) at 500 °C for 6 h and subsequent calcination at 500 °C for 6 h under dry air flow (45 mL/min). The final color of the calcined samples was brown, which turns to beige for the lower copper content.

The reduction experiments of Cu-MMS were performed by exposing of the samples under H_2 flow (70 mL/min) at 400 °C during 6 h with heating ramp of 1 °C/min.

Characterization Techniques. The materials were characterized by scanning electronic microscopy (SEM), transmission electronic microscopy (TEM), UV−vis diffuse reflectance (UV−vis-DR) spectroscopy, Fourier transform infrared spectroscopy with pyridine adsorption (FT-IR-pyr) and X-ray absorption spectroscopy (XAS). SEM micrographs were obtained in a JEOL model JSM 6380 LV. Lower resolution TEM images were obtained in a Jeol model JEM-1200 EXII System. UV−vis-DR spectra of the materials were recorded using a Perkin-Elmer precisely Lambda 35 spectrophotometer, to which a diffuse reflectance chamber Labsphere RSA-PE-20 with an integrating sphere of 50 mm diameter and internal Spectralon coating is attached. Once the solid samples were compacted in a Teflon sample holder to obtain a sample thickness of ∼2 mm, their spectra were recorded at 100 nm/min in the range 200−900 nm. Spectral grade $BaSO_4$ was used as the reference material. The spectra were taken in air at room temperature, and the data were automatically transferred according to the Kubelka−Munk equation: $f(R) = (1 - R_\infty)^2/2R_\infty$. FTIR spectral measurements of pyridine adsorption on the samples were performed on a JASCO FT-IR 5300 spectrometer equipped with a DTGS detector. The range and resolution of acquisition were 4600−400 and 4 cm^{-1}, respectively. A self-supporting wafer for each sample (∼20 mg and 13 mm of diameter) was prepared, placed in a thermostatized cell with CaF_2 windows connected to a vacuum line, and evacuated for 8 h at 400 °C. The background spectrum was recorded first after cooling the sample to room temperature. Afterward, the solid wafer was exposed to pyridine vapors (Sintorgan, 99% purity) until the system was saturated to ∼46 mmHg at room temperature; the contact time at this pressure was 12 h. The IR spectrum for each sample was obtained after pyridine desorption by evacuation for 1 h at 100−200 °C. All the spectra were recorded at room temperature before and after pyridine adsorption and desorption at each temperature. The difference spectrum was obtained finally by subtracting the background spectrum recorded previously.

Speciation Copper in Spherical Mesoporous Silicates

J. Phys. Chem. C, Vol. 114, No. 28, 2010 **12223**

TABLE 1: Chemical Composition and Structural Parameters of the Cu−MMS

sample	Si/Cu[a] (molar ratio)	Cu content[b] (wt %)	$a_0{}^c$ (nm)	$D_{BJH}{}^d$ (nm)	$t_w{}^e$ (nm)	V^f (cm³/g)	$S_{BET}{}^g$ (m²/g)
Cu−M(20)	20	9.45	4.36	2.63	1.73	0.972	834
Cu−M(60)	60	3.6	4.08	2.64	1.44	1.266	1158
Cu−M(240)	240	0.657	3.85	2.46	1.39	0.956	1112

[a] In synthesis gel. [b] In final solid. [c] Lattice parameter. [d] BJH pore diameter. [e] Wall thickness calculate by $a_0 - D_p$. [f] Total pore volume. [g] BET specific surface area.
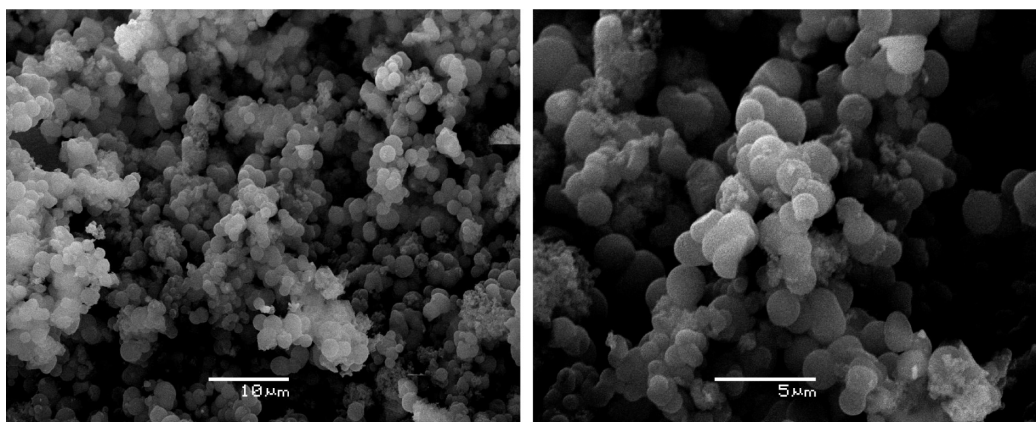
Figure 1. Scanning electron micrographs of Cu−M(60).

The Cu K-edge XANES/EXAFS experiments were performed at the D04B-XAS beamline at the LNLS (Laboratorio Nacional de Luz Sincrotron, Campinas, SP, Brazil), using a Si(111) single-crystal monochromator. The incident beam energy was of 1.37 MeV, with 1.2 eV resolution and harmonic contamination <1%.

The pellet samples were heat treated (300 °C for 6 h in a furnace with N_2 flow) and sealed with Kapton windows under inert gas. The XANES/EXAFS spectra of the Cu K-edge in catalyst and reference materials (Cu, Cu_2O, and CuO) were recorded at room temperature in the transmission mode. Photon energies were calibrated using a Cu foil by setting the first inflection point in its spectrum at the absorption edge (8979 eV).

EXAFS spectra were fitted by using the IFEFFIT[20] program using theoretical standards from ARTEMIS.[21] Background contributions were removed using the AUTOBK algorithm[22] (ATHENA program).[23] The Fourier transforms (FTs) of EXAFS signal have been obtained between $k_{min} = 2$ Å^{-1} and $k_{max} = 12$ Å^{-1}, using a Hanning window and corrected by theoretically calculated phase shifts (FEFF8 code).[24] The phase shifts and the amplitude functions used in the fitting routine were calculated using the FEFF code via CuO bulk crystallographic parameters.[25,26]

Results and Discussion

Table 1 summarizes the chemical composition and structural properties of the different samples prepared in this study. The XRD patterns and the N_2 adsorption/desorption isotherms, previously reported elsewhere,[19] are characteristic of mesoporous materials with well-defined MCM-41 type structure. It is noteworthy that even for copper content around 10 wt %, a good structural regularity was obtained. Very small CuO particles could be detected by large angle XRD, which are increased with the copper content in the initial gel. On the other hand, as the content of Cu is increased, the main peak corresponding to plane (100) shifted toward lower diffraction angles and an increment in the parameter a_0 is observed, consistently with a probable incorporation of Cu into the siliceous structure.

Our DR-UV−vis analysis previously performed[19] allows us to infer that copper is present on the mesoporous silica in the form of various species: isolated mononuclear $Cu^{\delta+}$ cations possibly in coordination with the lattice oxygen; linear oligo-nuclear $[Cu^{\delta+}\cdots O^{\delta-}\cdots Cu^{\delta+}]_n$ clusters possibly inserted into mesoporous channels; bulky CuO oxides segregated or occluded inside the secondary mesopores (CuO nanoparticles detectable by XRD).

Although the incorporation of Cu decreases the specific surface area (Table 1), all the catalysts possess large BET surface areas above 800 m²/g, which is characteristic of the mesoporous materials. However, the surface area reduction of the Cu−M(20) sample, prepared with higher Cu content, could be due to various causes, such as the intrapore formation of $[Cu^{\delta+}\cdots O^{\delta-}\cdots Cu^{\delta+}]_n$ clusters and/or enough small CuO nanoparticles (no detectable by XRD) finely dispersed within the mesopores, which is evidenced by the apparent increase in the wall thickness, the introduction of $Cu^{\delta+}$ ions into the MCM-41 framework, which lead to an increase in density of the composites, the blocking of pores of the meso-structure by bulky CuO oxides particles, and, finally, the less structural order due to the incorporation of copper into MCM-41 structure.[27]

The particle size and morphology of Cu−MMS were investigated by scanning electron microscopy. The SEM images of the Cu−M(60) representative sample are presented in Figure 1. As can be seen, these materials show spherical-like morphology in the micrometer range with a narrow particle-size distribution in the range between 2 and 3 μm. It is noteworthy that a substantial amount of fragments exist in the final Cu-MMS product, possibly due to time of hydrothermal treatment employed.[6] Nevertheless, this sample exhibits a well-resolved X-ray diffraction pattern.[19] Therefore, it will be expedient to independently optimize the particle morphology and the mesoporous structure characteristic of MCM-41 materials. On the other hand, Szegedi et al.[5] informed spherical morphology for samples Cu-MCM-41 also synthesized by direct incorporation. The aging of those samples was performed at room temperature of the synthesis gel and the particle diameter reported from TEM measurements was ≤0.5 μm. Therefore, it might be inferred
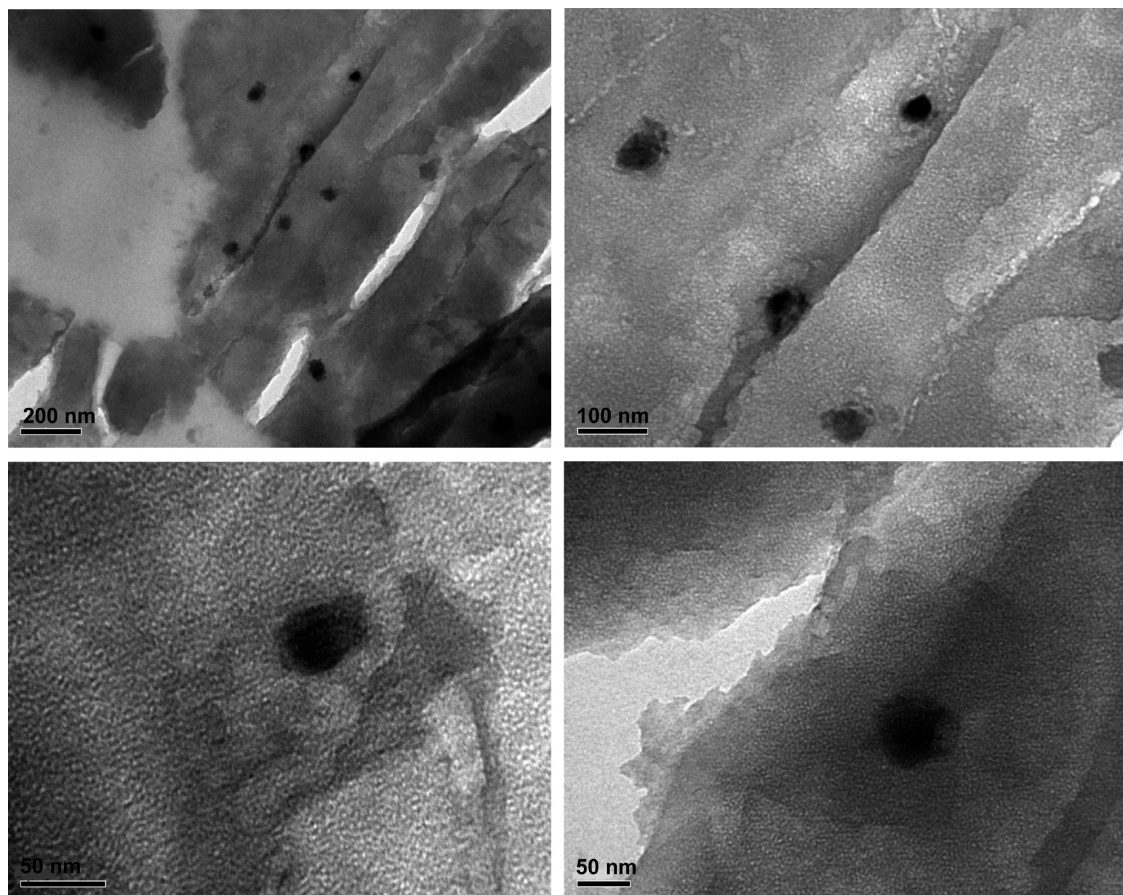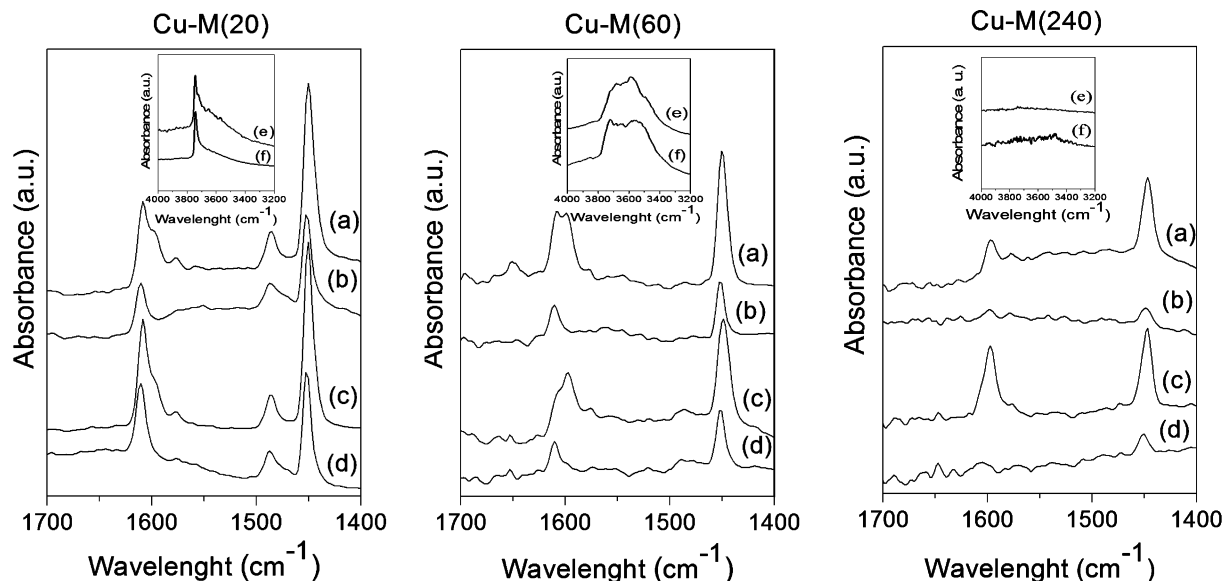
Figure 2. Transmission electron microscopy images of Cu−M(20).

that a hydrothermal treatment possibly promotes the ever-growing engine of these spherical particles.

Measurements of transmission electron microscopy of the Cu−MMS materials were made in order to examine their structural regularity. Figure 2 shows TEM images of sample Cu−M(20), taken as representative. As it is seen, these materials present a well-defined mesoporous structure. However, these micrographs do not show the typical hexagonal pore arrangement of MCM-41 type materials. On the other hand, this study also reveals the size distribution of the CuO nanoparticles. As it is can be observed in the micrographs, high-contrast regions randomly interrupt the pore arrangement characteristic of the mesoporous materials. These strong regions can be attributed to the presence of CuO nanoparticles that permeate the entire bulk. The obtained diameter is around 30 nm. Nanoparticles appear not agglomerated and totally occluded in the amorphous silica, possibly filling some of the secondary mesopores.[19] It is noteworthy that there were no segregated CuO on the external surface of silicate, in contrast with the results obtained from material modified with metal transitions prepared via wet impregnation or organofunctionalized.[28−33] In this regard, Lim et al.[34] evidenced the anchoring and the partial occlusion of metallic clusters on the pore walls of MCM-41.

Finally, in contrast to that reported by Li et al.,[27] we have just reported, besides the presence of CuO nanoparticles, the existence of nanoclusters $[Cu^{\delta+}\cdots O^{\delta-}\cdots Cu^{\delta+}]_n$, possibly inserted into mesoporous channels, and of $Cu^{\delta+}$ isolated species possibly in coordination with the lattice oxygen in these Cu-MMS.[19] These species have not been detected in these TEM micrographs probably due to very small size and the low resolution of the measuring equipment.

The chemisorption of pyridine followed by IR studies is usually a useful probe to detect the presence and nature of acid sites on a catalyst.[35] It is well-known that pyridine, as a basic molecule, can interact via the nitrogen lone-pair electrons with these acid sites, giving rise to characteristic bands. Information on the strength of Lewis and Brønsted acid sites can be obtained from pyridine thermodesorption. Figure 3 (curves a and b) shows FT-IR spectra of the calcined samples synthesized with different content of copper, recorded after the adsorption of pyridine and subsequent evacuation at 100 and 200 °C. It is known that pyridine would form hydrogen bonds with the silanol groups present in the structure whose hydroxyls are not capable to protonate pyridine. All the samples show a band corresponding to hydrogen bonded pyridine at 1599 cm^{-1},[36−40] which disappear upon evacuation at 200 °C indicating a weak interaction between pyridine and the SiOH groups of the structure and thus a weak acid strength. As can be observed, a band at 1608 cm^{-1}, corresponding to pyridine coordinately bonded to Lewis acid sites[36−42] is increased proportionally according to the amount of copper incorporated into the material. Moreover, the IR absorption band present at 1447 cm^{-1} could be interpreted in terms of the overlapping of both the hydrogen-bonded pyridine band and a band attributed to a Lewis-type adduct;[39] this band is also increased with growing copper content. Our samples do not show bands at 1540 and 1636 cm^{-1} characteristic of Brønsted acid sites.[41,43−45] Therefore, the band observed at 1490 cm^{-1}, frequently assigned to pyridine associated with both, Lewis and Brønsted acid sites, in our samples, corresponds only to Lewis acid sites. Again, this band is also increased when the copper content increases. Judging by the presence of their

Speciation Copper in Spherical Mesoporous Silicates

*J. Phys. Chem. C, Vol. 114, No. 28, 2010* **12225**

Figure 3. FTIR of pyridine adsorbed on the calcined Cu-MMS modified with different copper content, after desorption at 100 °C (a) and 200 °C (b) and the reduced Cu-MMS under H_2 flow, after desorption at 100 °C (c) and 200 °C (d), respectively. Inserted in spectrum of each sample is the region of OH before pyridine adsorption of the samples (e) and reduced samples (f).

characteristic bands, these Lewis acid sites are strong enough to retain the pyridine molecules until 200 °C.

In order to attempt to determine the possible origin of such Lewis acidity, the acidity of the samples was again measured after a reduction treatment was performed. Note here that the reduction conditions (H_2 flow = 70 mL/min; 400 °C) employed allowed a complete reduction of both the oligonuclear $[Cu^{\delta+}\cdots O^{\delta-}\cdots Cu^{\delta+}]_n$ clusters and bulky CuO oxides, as evidenced from TPR studies.[19] Thus, Figure 3 (curves c and d) shows FT-IR spectra of theses reduced samples recorded after the adsorption of pyridine and subsequent evacuation at 100 and 200 °C. As observed the spectra of the reduced samples are very similar to those from nonreduced samples. Therefore, it is possible to suggest that the incorporation of copper into the silica framework generates Lewis acid sites on the surface which increases with copper content. The origin of these sites can be mainly attributed to the presence of isolated copper species possibly coordinated to framework oxygen atoms.

In addition, the DR-UV–vis spectra of these reduced samples are show in Figure 4. As it is known, metallic copper species absorb in the 225–590 nm range giving an absorption maximum at 570–590 nm corresponding to the conduction band.[46,47] Thus, the presence of a strong band at 570–575 nm in our samples would be indicating the presence of Cu^0 and corroborating the effective reduction of the species $[Cu^{\delta+}\cdots O^{\delta-}\cdots Cu^{\delta+}]_n$ and CuO, observed by TPR.[19] The absence of the absorption band between 600 and 800 nm shows the complete reduction of CuO nanoparticles. Moreover, since that oligonuclears clusters are reduced to approximately 310 °C, according to the TPR results,[19] a overlapped absorption corresponding to them in these spectra can be discarded. However, in the UV range, the $Cu^{2+} \leftarrow O^{2-}$ charge transfer transitions and the $d^{10}-d^9s^1$ transition of Cu^+, both corresponding to isolated species (nonreducible), as well as the $d^{10}4s-d^{10}4p$ transition of Cu^0 could be superimposed.[19,46] This is confirmed by the spectrum of the reduced sample Cu–M(240), which clearly presents an absorption band in the UV range. Besides, given the low concentration of clusters and oxides present in the calcined sample, a very weak absorption around 570 nm due to Cu^0 could be observed in this reduced sample.[19]
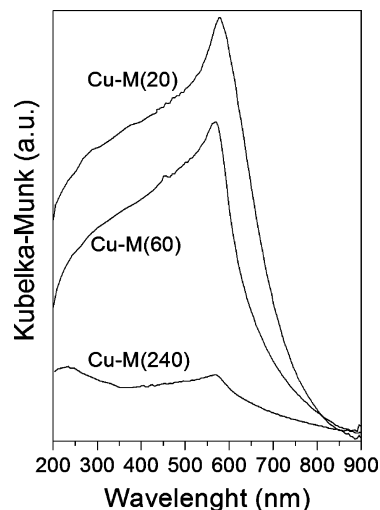
Figure 4. UV–vis diffuse reflectance spectra of the reduced Cu-MMS.

Moreover, it is noteworthy that the low-angle XRD patterns of these reduced samples (not shown here) were very similar to those of calcined samples previously reported,[19] indicating that the reduction treatment does not affect the structural order.

Continuing with the FTIR analysis, Figure 3 also shows the IR spectra in the hydroxyl range of the calcined and reduced samples before pyridine adsorption. In the spectrum of the sample Cu–M(20), modified with the highest copper content, one can clearly see the presence of the band at approximately 3740 cm^{-1} corresponding to the v(O–H) stretching vibrations of isolated terminal hydroxyl groups.[48–53] Meanwhile, for the sample Cu–M(60), with molar ratio Si/Cu = 60, new bands around 3680 and 3640 cm^{-1} appear, which could be attributed to the presence of Cu–OH surface species.[48,49,51] A broad contribution between 3700 and 3200 cm^{-1}, assigned to hydrogen-bonded hydroxyls derived from internal and defective Si–OH groups,[54] is also present. Thus, this band appears possibly due to the interaction between vicinal OH groups, as Si–OH and Cu–OH groups are present in this sample. For the sample Cu–M(240), modified with the lower copper content, it is possible to observe that the band corresponding to the terminal

SCHEME 1: Possible Interactions of Cu$^{\delta+}$ Isolated Species with Silica Structure
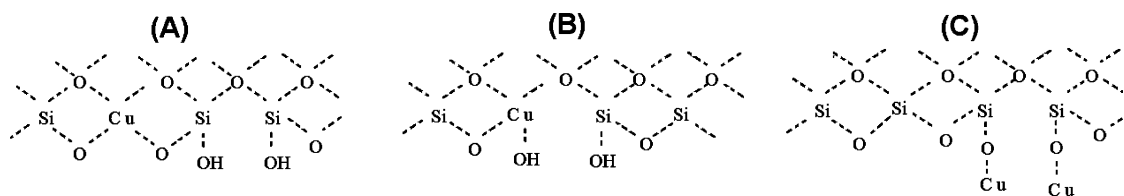
silanol groups became invisible likely due to the coordination of the Si−OH groups with copper ions.[50]

In this context, Lamberti et al.[55] suggest that in the incorporation mechanism the Ti atoms in the MFI framework occur via the insertion of Ti in the defective sites (Si vacancy) of silicate. They also reported that the incorporation of Ti into this zeolite framework causes a progressive decrease in hydrogen-bonded hydroxyls.

According to the last results, we can propose three structures of isolated copper species, which are shown in Scheme 1. Thus, for the sample Cu−M(20), the clear presence of both the terminal SiOH groups and the Lewis acid sites jointly with the absence of the band between 3700 and 3200 cm^{-1}, allows us to suggest that these sites could be arising from copper atoms bonded to four framework oxygen atoms (species A). Meanwhile for the sample Cu−M(60), the copper could also be located in terminal positions Cu−OH (species B), judging by the broad band between 3700 and 3200 cm^{-1}. Finally, in the case of the sample Cu−M(240) with the lower Cu content, the Si−OH groups could be likely blocked after the condensation with the Cu species leading to the formation of Si−O−Cu bonds (species C).

In order to investigate the local environment of Cu in copper species already presented here,[19] X-ray absorption (XAS) measurements were performed on these Cu-MMS.

The pre-edge and XANES regions of the absorption spectra contain electronic information on the local environment of the absorbing atom which can be analyzed to extract their symmetry. Additionally, examination of the edge shifting of XANES spectra provides direct information on the average oxidation state of copper. The origin of the Cu K XANES features was reported by Groothaert et al.[56] XANES spectra of the model compounds CuO, Cu$_2$O, and Cu foil are showed in Figure 5. A weak peak at 8977.6 eV can be distinguished for CuO. This peak is associated with the formally dipole-forbidden Cu(II) 1s → 3d electronic transition and is recognized as the fingerprint of bivalent Cu in a nonsymmetric center,[57] being predominantly quadrupolar in CuO.[58] In principle, this transition is forbidden by dipole selection rules and hence a weak one. However its intensity is higher when the first coordination shell lacks inversion symmetry, which is the case for tetrahedral (T_d) environments but not octahedral (O_h) or tetragonal (D_{4h}) environments. Then, the very low intensity of this transition is consistent with a centrosymmetric copper environment, for example, tetragonally distorted octahedral.
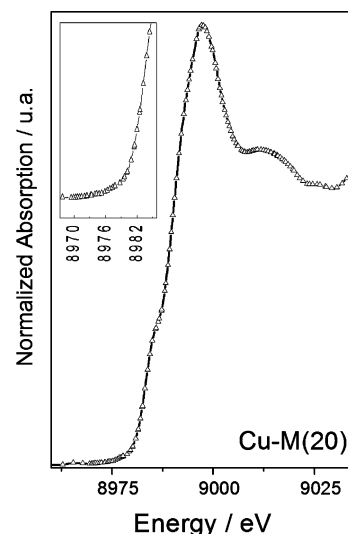
The dipole-allowed Cu(II) 1s → 4p transitions contribute to the intensity at the region between 8995 and 8998 eV in the absorption spectrum. In the case of the tetragonal-distorted octahedral symmetry of Cu(II) in CuO, the 1s → 4p$_z$ transition shifts to lower energy, resulting in a clear shoulder at 8986 eV as can be seen in Figure 5. Similarly, the 1s → 4p transitions in tetrahedral Cu(I) compounds are all above 8986 eV, whereas two- and three-coordinated Cu(I) compounds have the 1s → 4p absorption feature at the 8983−8986 eV region.[59] Cu(I) in Cu$_2$O possesses a linear two-coordinated structure, and consequently

a sharp peak located at 8981.5 eV is observed. Metallic Cu exhibits also a near-edge feature around 8982 eV. However, the resonance features above the edge jump are clearly different from those of Cu$_2$O, as can be seen in Figure 5.

The XANES spectrum of the sample Cu−M(20) (modified with ∼10 wt % of Cu) is shown in Figure 6. This sample shows a shoulder at ∼8985 eV which can be attributed to both the 1s → 4p$_z$ transition for tetragonal Cu(II) in CuO and the 1s → 4p transition for two- and three-coordinated Cu(I) compounds, likely linear Cu−O−Cu clusters. It should be noted that the transition at ∼8977 eV characteristic of copper(II) compounds
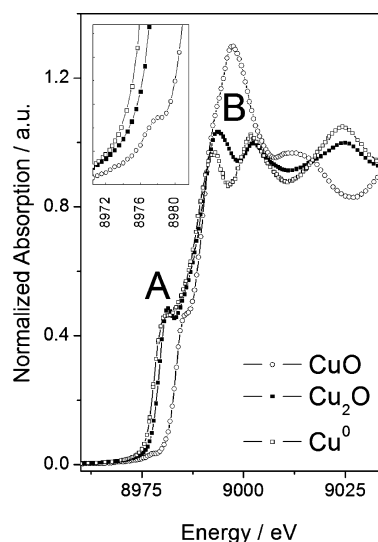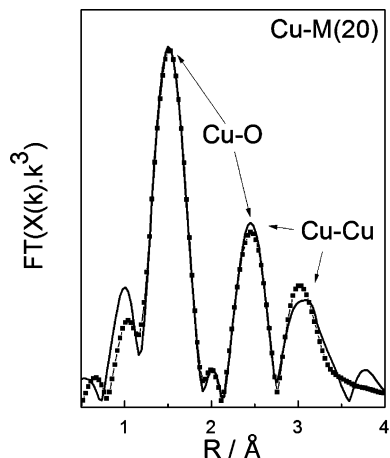

Figure 5. Cu K XANES spectra for reference compounds metallic Cu, Cu$_2$O, and CuO. Note the difference between Cu$_2$O and CuO in the region corresponding to 1s → 3d transitions or dipolar forbidden transition (A), and 1s → 4p transition (B).

Figure 6. Cu K XANES spectra for sample Cu−M(20).

Speciation Copper in Spherical Mesoporous Silicates

J. Phys. Chem. C, Vol. 114, No. 28, 2010 **12227**

Figure 7. The Fourier transform of the EXAFS signal $\chi(k)k^3$ for the sample Cu−M(20) (black line) and the best fitting of EXAFS spectra (line, +; symbol, ■).

TABLE 2: EXAFS Analysis Results for Cu−M(20)[a]

sample	shell	N	R (Å)	σ^2 (Å^{-2})	E_{shift} (eV)
Cu−M(20)	Cu−O	2.29_5	1.92_5	0.019_5	0.85_5
	Cu−O	1.91_5	1.98_5	0.019_5	0.85_5
	Cu−O	2.21_5	2.79_5	0.019_5	0.85_5
	Cu−Cu	3.90_5	2.90_5	0.010_5	0.85_5
	Cu−Cu	3.69_5	3.09_5	0.010_5	0.85_5
	Cu−Cu	2.10_5	3.19_5	0.010_5	0.85_5

[a] Key: N, average coordination number; R, distance; σ^2, Debye−Waller factor; E_0, refined correction to the threshold energy of the absorption edge.

could not be detected in this sample. This feature could be explained by taking into account that an important fraction of Cu(II) used in the preparation of the synthesis gel is autoreduced to Cu(I) under the synthesis conditions, as it is evidenced by XPS.[19] In addition, the lack of a sharp peak at 8981.5 eV provides clear evidence that the Cu_2O and Cu(0) phases are absent in the Cu−M(20) sample.

On the other hand, the presence of the pre-edge shoulder in the Cu−M(20) sample is not necessarily incompatible with a framework sitting of copper, although the lack of a detectable peak at around 8977 eV could indicate that copper is not tetrahedrally coordinate. When copper is incorporated into an initially tetrahedral framework site, bonded with four oxygen atoms, the metal site is distorted rather than adopt a tetrahedral site, as reported for CuAPO-5.[57,60] Thus, the flexibility of the framework could tolerate tetragonally distorted copper as in the case of microporous material CuAPO-5.[57,60,61] Therefore, the presence of framework and extra-framework copper as well as the coexistence of both Cu^{2+} and Cu^+ oxidation states, recently proposed by us,[19] can be confirmed by these results.

EXAFS spectra of copper can provide information on the local atomic arrangement including bond distance, number of near-neighbors, and thermal disorder. EXAFS spectra of Cu-MMS were recorded and analyzed in the k range between 2 and 12 Å^{-1}. Figure 7 shows the magnitude of the Fourier transform without phase correction of Cu K-edge EXAFS signal (multiplied by k^3) for the sample Cu−M(20) (modified with ∼10 wt %) and the best fitting of EXAFS data. This spectrum shows three main peaks at 1.51, 2.46, and 3.10 Å. In order to quantitatively analyze these data, these main peaks were isolated and fitted using standard procedures. Theoretical standards were generated by the FEFF code via CuO bulk crystallographic parameters. For all the analyzed data, the Debye−Waller factors (σ^2) were less than 0.02 Å (constrained to be the same than Cu−O and Cu−Cu shells). Table 2 summarizes structural parameters of copper species extracted from the best-fitted EXAFS data. As can be seen, Cu atoms present a multiplicity of approximately 4.2 for the Cu−O distances ranging between 1.92 and 1.98 Å, probably representing a square-planar arrangement, besides another Cu−O contribution at 2.79 Å with average coordination number of 2.21, probably representing the axial bonds of a distorted octahedron. These parameters are very similar to those obtained from CuO bulk.[57,60] However, it is noteworthy that the adjustment obtained in the data reduction is not completely confident. This uncertainty is associated with

the use of not completely transferable reference compounds for this analysis. Additional contributions to the EXAFS signal that are not strictly due to the EXAFS signal of CuO, as the corresponding Cu−(O−Cu)−Si and/or Cu−(O)−Cu species, are presented in these type of samples.[62,63] However, under the measurement conditions (*RT* at atmospheric pressure) these species could not be observed. Continuing with the EXAFS analysis, all the distances (equatorial and axial ones) could be resolved because of their relatively small Debye−Waller factors. In this respect, Nilsen[64] observed in copper-incorporated SnAPO-5 materials a tetragonal-distorted octahedron, in which the Debye−Waller factors of Cu−O are small and the axial distances are clearly resolved. These authors state that this is possibly due to a framework substitution of copper since the porous materials are very flexible and because a lowering of the symmetry at the T-atom position could be more favored than for copper to occupy a tetrahedral site.[60] On the other hand, Mathisen et al.[57] suggested that the presence of a peak at 3.1 Å in the EXAFS spectra of a zeo-type lattice is a fingerprint for framework substitution. Thus, we could infer that the copper would also be incorporated into the framework in a distorted octahedral environment, besides in the CuO phase. In addition, a light increase in the overall coordination number to oxygen atoms ($N = 6.41$) with respect to CuO ($N = 6.00$),[57,60] could also suggest that some copper is incorporated into the framework. On the other hand, different coordinations of copper in CuAPO-5 were reported by Muñoz et al.[65] where copper can adopt four-, five-, or six-coordinated positions depending on the number of extra-framework species. A copper complex confined within the pores is ready to interact with both framework and extra-framework oxygen atoms.[66] In this sense, Hamada et al.[67] were the first to suggest the contribution of a Cu⋯Cu local structure in the EXAFS spectra of typical overexchanged samples, active for NO decomposition. Using fitting techniques, Grünert et al.[68] deduced a Cu⋯Cu distance of ∼2.95 Å from the EXAFS data of overexchanged samples and assigned it to small clusters with the copper atoms linked by extra-lattice-oxygen species. Kuroda et al.[69] and Palomino et al.[70] assigned the contribution at about ∼2.75 Å in their EXAFS spectra of evacuated highly exchanged samples to the presence of Cu^+⋯Cu^+ pairs. As can be seen in Table 2, we found that sample Cu−M(20) has Cu⋯Cu distances of 2.90, 3.09, and 3.19 Å, with coordination numbers of 3.90, 3.69, and 2.10, respectively. A decrease in the Cu−Cu overall coordination number ($N = 9.69$) with respect to CuO ($N = 12.00$),[57,60] in particular for the two first shells, provides further evidence for the presence of copper species with low coordination number, like oligomeric copper species.[53] In conclusion, the average coordination numbers observed in our samples could result from a mixture of copper nanosized species: segregated CuO nano-oxides besides isolated $Cu^{\delta+}$ cations located into framework with oligonuclear clusters like $[Cu^{\delta+}\cdots O^{\delta-}\cdots Cu^{\delta+}]_n$ in its surroundings, confined within the pores.

Conclusions

Mesoporous silicate particles with spherical morphology containing nanosized copper species were synthesized by conventional hydrothermal synthesis. The Cu-MMS showed a narrow particle-size distribution in the range between 2 and 3 μm. TEM images of these materials showed a well-defined mesoporous structure. However, the micrographs do not show the typical hexagonal pore arrangement of MCM-41 type materials. Additionally, CuO nano-oxides of diameter ~30 nm occluded in the amorphous silica, possibly filling some secondary mesoporosity, also were detected. A detailed study about the relationship between copper loading degree and the acid properties with the local isolated $Cu^{\delta+}$ species surroundings was performed through IR-TF-Py and DR-UV−vis spectroscopy measurements together with reduction experiments under H_2 flow. The incorporation of copper into the silica framework generated surface Lewis acid sites which increased with copper content. These sites could be attributed to the presence of isolated $Cu^{\delta+}$ species possibly coordinated to framework oxygen atoms. It is noteworthy that Brønsted acid sites were not detected in our materials. From the performed characterization results, three tentative positions of isolated $Cu^{\delta+}$ species were proposed by us. From a detailed analysis of XANES spectra, we could infer the coexistence of copper states (+1 and +2) in the species of these materials. Finally, the average coordination numbers calculated from EXAFS experiments, could result from a mixture of copper nanosized species: CuO nanoparticles besides isolated $Cu^{\delta+}$ cations located into framework with oligonuclear clusters like $[Cu^{\delta+}\cdots O^{\delta-}\cdots Cu^{\delta+}]_n$ in its surroundings, confined within the pores.

References and Notes

(1) Beck, J. S.; Vartuli, J. C.; Roth, W. J.; Leonowicz, M. E.; Kresge, C. T.; Schmidt, K. D.; Chu, C. T. W.; Olson, D. H.; Sheppard, E. W.; McCullen, S. B.; Higgins, J. B.; Schlenker, J. L. *J. Am. Chem. Soc.* **1992**, *114*, 10834.

(2) Kresge, C. T.; Leonowicz, M. E.; Roth, W. J.; Vartuli, J. C.; Beck, J. S. *Nature* **1992**, *359*, 710.

(3) Huang, Y. J.; Wang, H. P.; Lee, J. F. *Appl. Catal., B* **2003**, *40*, 111.

(4) Grün, M.; Lauer, I.; Unger, K. K. *Adv. Mater.* **1997**, *9*, 254.

(5) Szegedi, Á.; Kónya, Z.; Méhn, D.; Solymár, E.; Pál-Borbély, G.; Horváth, Z. E.; Biró, L. P.; Kiricsi, I. *Appl. Catal., A* **2004**, *272*, 257.

(6) Liu, X.; Sun, H.; Chen, Y.; Yang, Y.; Borgna, A. *Microporous Mesoporous Mater.* **2009**, *121*, 73.

(7) Kummer, J. T. *Prog. Energy Combust. Sci.* **1980**, *6*, 177.

(8) Kreuzer, T.; Lox, E. S.; Lindner, D.; Leyrer, J. *Catal. Today* **1996**, *29*, 17.

(9) Mccabe, R. W.; Mitchell, P. J. *Appl. Catal.* **1988**, *44*, 73.

(10) Wong, C.; McCabe, R. W. *J. Catal.* **1989**, *119*, 47.

(11) Liu, C. C.; Teng, H. *Appl. Catal., B* **2005**, *58*, 69.

(12) Gervasini, A.; Bennici, S.; Auroux, A.; Guimon, C. *Appl. Catal., A* **2007**, *331*, 129.

(13) Bennici, S.; Auroux, A.; Guimon, C.; Gervasini, A. *Chem. Mater.* **2006**, *18*, 3641.

(14) Ramallo-López, J. M.; Lede, E. J.; Requejo, F. G.; Rodríguez, J.; Kim, J. Y.; Rosas-Salas, R.; Domínguez, J. M. *J. Phys. Chem. B* **2004**, *108*, 20005.

(15) Nilsen, M. H.; Antonakou, E.; Bouzga, A.; Lappa, A.; Mathisen, K.; Stöcker, M. *Microporous Mesoporous Mater.* **2007**, *105*, 189.

(16) Liu, D. J.; Robota, H. J. *J. Phys. Chem. B* **1999**, *103*, 2755.

(17) Groothaert, M. H.; van Bokhoven, J. A.; Battiston, A. A.; Weckhuysen, B. M.; Schoonheydt, R. A. *J. Am. Chem. Soc.* **2003**, *125*, 7629.

(18) Mathisen, K.; Nicholson, D. G.; Fitch, A. N.; Stockenhuberc, M. *J. Mater. Chem.* **2005**, *15*, 204.

(19) Chanquía, C. M.; Sapag, K.; Rodríguez-Castellón, E.; Herrero, E. R.; Eimer, G. A. *J. Phys. Chem. C* **2010**, *114*, 1481.

(20) http://cars9.uchicago.edu/ifeffit/About.

(21) http://cars9.uchicago.edu/~ravel/software/aboutartemis.html.

(22) Newville, M.; Livins, P.; Yacoby, Y.; Rehr, J. J.; Stern, E. A. *Phys.Rev. B* **1993**, *47*, 14126.

(23) http://cars9.uchicago.edu/~ravel/software/aboutathena.html.

(24) http://leonardo.phys.washington.edu/feff/. Ankudinov, A. L.; Ravel, B.; Rehr, J. J.; Conradson, S. D. *Phys. Rev. B* **1998**, *58*, 7565.

(25) http://cars9.uchicago.edu/cgi-bin/atoms/Atoms-Search.cgi.

(26) http://cars9.uchicago.edu/cgi-bin/atoms/atoms.cgi.

(27) Li, Z.; Gao, L. *J. Phys. Chem. Solids* **2003**, *64*, 223.

(28) Ajaikumar, S.; Pandurangan, A. *Appl. Catal., A* **2009**, *357*, 184.

(29) Yin, D.; Li, W.; Yang, W.; Xiang, H.; Sun, Y.; Zhong, B.; Peng, S. *Microporous Mesoporous Mater.* **2001**, *47*, 15.

(30) Hao, X. Y.; Zhang, Y. Q.; Wang, J. W.; Zhou, W.; Zhang, C.; Liu, S. *Microporous Mesoporous Mater.* **2006**, *88*, 38.

(31) Bourlinos, A. B.; Simopoulos, A.; Boukos, N.; Petridis, D. *J. Phys. Chem. B* **2001**, *105*, 7432.

(32) Lensveld, D. J.; Mesu, J. G.; Van Dillen, A. J.; de Jong, K. P. *Microporous Mesoporous Mater.* **2001**, *44−45*, 401.

(33) Hartmann, M.; Racouchot, S.; Bischof, C. *Microporous Mesoporous Mater.* **1999**, *27*, 309.

(34) Lim, S.; Wang, C.; Yang, Y.; Ciuparu, D.; Pfefferle, L.; Haller, G. L. *Catal. Today* **2007**, *123*, 122.

(35) Eimer, G. A.; Casuscelli, S. G.; Chanquía, C. M.; Elías, V.; Crivello, M. E.; Herrero, E. R. *Catal. Today* **2008**, *133−135*, 639.

(36) Trong On, D.; Nguyen, S.; Hulea, V.; Dumitriu, E.; Kaliaguine, S. *Microporous Mesoporous Mater.* **2003**, *57*, 169.

(37) Srinivas, D.; Srivastava, R.; Ratnasamy, P. *Catal. Today* **2004**, *96*, 127.

(38) Chakraborty, B.; Viswanathan, B. *Catal. Today* **1999**, *49*, 253.

(39) Sakthivel, A.; Dapurkar, S.; Gupta, N.; Kulshreshtha, S.; Selvam, P. *Microporous Mesoporous Mater.* **2003**, *65*, 177.

(40) Conesa, T.; Hidalgo, J.; Luque, R.; Campelo, J.; Romero, A. *Appl. Catal., A* **2006**, *299*, 224.

(41) Otero Areán, C.; Rodríguez Delgado, M.; Montouillout, V.; Lavalley, J.; Fernández, C.; Cuart Pascual, J.; Parra, J. *Microporpus Mesoporous Mater.* **2004**, *67*, 259.

(42) Cedeño, L.; Hernández, D.; Klimova, T.; Ramírez, J. *Appl. Catal., A* **2003**, *241*, 39.

(43) Escalona Platero, E.; Peñarroya Mentruit, M.; Otero Areán, C.; Zecchina, A. *J. Catal.* **1996**, *162*, 268.

(44) Morterra, C.; Magnacca, G. *Catal. Today* **1996**, *27*, 497.

(45) Chen, L.; Noreña, L.; Navarrete, J.; Wang, J. *Mater. Chem. Phys.* **2006**, *97*, 236.

(46) Praliaud, H.; Mikhailenko, S.; Chajar, Z.; Primet, M. *Appl. Catal., B* **1998**, *16*, 359.

(47) Kobayashi, Y.; Ishida, S.; Ihara, K.; Yasuda, Y.; Morita, T.; Yamada, S. *Colloid Polym. Sci.* **2009**, *287*, 877.

(48) Gao, F.; Zhang, Y.; Wan, H.; Kong, Y.; Wu, X.; Dong, L.; Li, B.; Chen, Y. *Microporous Mesoporous Mater.* **2008**, *110*, 508.

(49) Segura, Y.; Cool, P.; Kustroeski, P. P.; Chmielarz, L.; Dziembaj, R.; Vansant, E. F. *J. Phys. Chem. B* **2005**, *109*, 12071.

(50) Hao, X. Y.; Zhang, Y. Q.; Wang, J.; Zhou, W.; Zhang, C.; Liu, S. *Microporous Mesoporous Mater.* **2005**, *88*, 38.

(51) Anpo, M.; Matsuoka, M.; Shioya, Y.; Yamashita, H.; Giamello, E.; Monterra, C.; Che, M.; Patterson, H. H.; Webber, S.; Ouellette, S.; Fox, M. A. *J. Phys. Chem.* **1994**, *98*, 5744.

(52) Chmielarz, L.; Kustrowski, P.; Dziembaj, R.; Cool, P.; Vansant, E. F. *Appl. Catal., B* **2006**, *62*, 369.

(53) Babich, I. V.; Plyuto, Y. V.; Van der Voort, P.; Vansant, E. F. *J. Colloid Interface Sci.* **1997**, *189*, 144.

(54) Tamura, M.; Chaikittisilp, W.; Yokoi, T.; Okubo, T. *Microporous Mesoporous Mater.* **2008**, *112*, 202.

(55) Lamberti, C.; Bordiga, S.; Zecchina, A.; Artioli, G.; Marra, G.; Sapano, G. *J. Am. Chem. Soc.* **2001**, *123*, 2204.

(56) Groothaert, M. H.; van Bokhoven, J. A.; Battiston, A. A.; Weckhuysen, B. M.; Schoonheydt, R. A. *J. Am. Chem. Soc.* **2003**, *125*, 7629.

(57) Mathisen, K.; Nicholson, D. G.; Fitch, A. N.; Stockenhuberc, M. *J. Mater. Chem.* **2005**, *15*, 204.

Speciation Copper in Spherical Mesoporous Silicates

J. Phys. Chem. C, Vol. 114, No. 28, 2010 **12229**

(58) Bocharov, S.; Kirchner, Th.; Dräger, G.; Sipr, O.; Simunek, A. *Phys. Rev. B* **2001**, *63*, 045104.

(59) Kau, L. S.; Spira-Solomon, D. J.; Penner-Hahn, J. E.; Hodgson, K. O.; Solomon, E. I. *J. Am. Chem. Soc.* **1987**, *109*, 6433.

(60) Nicholson, D. G.; Merete, H. N. *J. Mater. Chem.* **2000**, *10*, 1965.

(61) Nilsen, M. H.; Antonakou, E.; Bouzga, A.; Lappa, A.; Mathisen, K.; Stöcker, M. *Microporous Mesoporous Mater.* **2007**, *105*, 189.

(62) Huang, Y.-J.; Wang, H. P.; Lee, J. F. *Chemosphere* **2003**, *50*, 1035.

(63) Liu, C. C.; Teng, H. *Appl. Catal., B* **2005**, *58*, 69.

(64) Nilsen, M. H. Ph.D. thesis, Norwegian University of Science and Technology, Department of Chemistry, 2000.

(65) Muñoz, T.; Prakash, A. M.; Kevan, L.; Balkus Jr., K. J. *J. Phys. Chem. B* **1998**, *102*, 1379.

(66) Huang, H. L.; Wang, H. P. *J. Electron Spectrosc. Relat. Phenom.* **2005**, *144*, 307.

(67) Hamada, H.; Matsubayashi, N.; Shimada, H.; Kintaichi, Y.; Ito, T.; Nishijima, A. *Catal. Lett.* **1990**, *5*, 189.

(68) Grünert, W.; Hayes, N. W.; Joyner, R. W.; Shpiro, E. S.; Siddiqui, M. R. H.; Baeva, G. N. *J. Phys. Chem.* **1994**, *98*, 10832.

(69) Kuroda, Y.; Kumashiro, R.; Yoshimoto, T.; Nagao, M. *Phys. Chem. Chem. Phys.* **1999**, *1*, 649.

(70) Palomino, G. T.; Fisicaro, P.; Bordiga, S.; Zecchina, A.; Giamello, E.; Lamberti, C. *J. Phys. Chem. B* **2000**, *104*, 4064.